materials

MDPI

Article

Corrosion Products Formed on MgZr Alloy Embedded in Geopolymer Used as Conditioning Matrix for Nuclear Waste—A Proposition of Interconnected Processes

Rémi Boubon [1], Jaysen Nelayah [2], Samuel Tardif [3], Xavier Deschanels [1] and Diane Rébiscoul [1,*]

[1] ICSM, CEA, CNRS, ENSCM, Université Montpellier, Marcoule, 30207 Bagnols-sur-Cèze, France; remi.boubon@cea.fr (R.B.); xavier.deschanels@cea.fr (X.D.)
[2] Laboratoire Matériaux et Phénomènes Quantiques, Université de Paris, CNRS, 75013 Paris, France; jaysen.nelayah@u-paris.fr
[3] CEA, IRIG-MEM, Université Grenoble Alpes, F-38000 Grenoble, France; samuel.tardif@cea.fr
* Correspondence: diane.rebiscoul@cea.fr

Abstract: Geopolymer has been selected as a hydraulic mineral binder for the immobilization of MgZr fuel cladding coming from the dismantling of French Uranium Natural Graphite Gas reactor dedicated to a geological disposal. In this context, the corrosion processes and the nature of the corrosion products formed on MgZr alloy in a geopolymer matrix with and without the corrosion inhibitor NaF have been determined using a multiscale approach combining in situ Grazing Incidence hard X-ray Diffraction, Raman microspectroscopy, Scanning and Transmission Electron Microscopies coupled to Energy Dispersive X-ray Spectroscopy. The composition, the morphology, and the porous texture of the corrosion products were characterized, and the effect of the corrosion inhibitor NaF was evidenced. The results highlighted the formation of $Mg(OH)_{2-x}F_x$. In addition, in presence of NaF, $NaMgF_3$ forms leading to a decrease of the thickness and the porosity of the corrosion products layer. Moreover, a precipitation of magnesium silicates within the porosity of the geopolymer was evidenced. Finally, we propose a detailed set of interconnected processes occurring during the MgZr corrosion in the geopolymer.

Keywords: magnesium corrosion; geopolymer; corrosion products; corrosion inhibitor; interconnected processes

Citation: Boubon, R.; Nelayah, J.; Tardif, S.; Deschanels, X.; Rébiscoul, D. Corrosion Products Formed on MgZr Alloy Embedded in Geopolymer Used as Conditioning Matrix for Nuclear Waste—A Proposition of Interconnected Processes. *Materials* **2021**, *14*, 2017. https://doi.org/10.3390/ma14082017

Academic Editor: Herman Potgieter

Received: 15 March 2021
Accepted: 8 April 2021
Published: 16 April 2021

1. Introduction

In France, the dismantling of French Uranium Natural Graphite Gas reactor [1] (UNGG) resulted in MgZr alloy fuel cladding waste containing uranium and fission product residues. Regarding the presence of these residues, MgZr fuel cladding is considered as an intermediate-level radioactive waste meant for geological disposal. Before their disposal, these waste materials have to be immobilized in a conditioning matrix, e.g., a hydraulic mineral binder.

Magnesium alloy is reactive regarding its corrosion in a hydraulic binder, leading to hazardous hydrogen production detrimental regarding the disposal safety. To limit hydrogen release, a geopolymer matrix has been selected as a potential mineral binder. A geopolymer is a nanoporous aluminosilicate filled with a basic poral solution (pH = 12) consisting of an alkaline solution and mainly hydrolyzed silica species [2]. This inorganic material is formed by a geopolymerization process corresponding to dissolution-recondensation reactions of dissolved species followed by inorganic polycondensation reactions [3]. This matrix presents interesting mechanical and chemical properties and has been largely studied for radioelement immobilization [4–7] such as ^{133}Cs [8] and ^{90}Sr [9], and the stabilization of radioactive liquid oily waste [10].

In geopolymer, when the basic poral solution is in contact with MgZr, Brucite $Mg(OH)_2$ is formed and limits the alloy corrosion [11,12]. Moreover, corrosion inhibitor additives can

be considered, such as NaF that favors the formation of fluorine phases, e.g., $Mg(OH)_{2-x}F_x$, MgF_2, $Na(K)MgF_3$, as proposed or characterized in [13–17], and that not modifies the geopolymer properties. These fluorine phases also limit the MgZr corrosion and thus the hydrogen production [18–20]. Recently, using electrochemical experiments, the corrosion of MgZr alloy embedded within the geopolymer with various NaF contents have shown that the corrosion rate and the nature of the fluorine phases formed are dependent of NaF concentration within geopolymer [21]. This result is in line with our recent experiments of natural MgZr alloy corrosion in poral solutions extracted from geopolymers with and without NaF [17]. The identification of the corrosion products (CP) formed has highlighted that the amounts of fluoride species and dissolved silica in the solution set the nature of the CP, i.e., Brucite, fluorine phases, and magnesium silicates, and probably their protective properties regarding the MgZr corrosion. However, the origin of these protective properties probably in relation with the CP porous texture have not been investigated. Moreover, in our experiments, magnesium silicates precipitation was observed within the CP layer contrary to the electrochemical experiments of Barros et al. [21].

Thus, the aim of this work is to study the nature, the porous texture, and the location of the CP formed during the corrosion of the MgZr alloy embedded in a geopolymer, with or without corrosion inhibitor NaF, and the underlying processes of their formation. To reach this goal, we used a multiscale approach combining in situ Grazing Incidence hard X-ray Diffraction (GI-XRD), Raman microspectroscopy, Scanning and Transmission Electron Microscopies coupled to Energy Dispersive X-ray Spectroscopy (SEM-EDX and STEM-EDX).

2. Materials and Methods

2.1. Materials

Magnesium alloys (Magnesium: 99.5% and Zirconium 0.5 wt%, referred as MgZr) ingots of 100 × 50 × 30 mm^3 supplied by Neyco Society (Vanves, France) were used in this study. The impurities present in the alloy are displayed in Table 1. This composition is close to the one used in the UNGG cladding.

Table 1. Impurities in MgZr (data supplied by Neyco).

Impurities	Al	As	Co	Cr	Cu	Fe	Mn	Ni	Sb	Zn	Cl
Quantity (ppm)	<10	<20	<10	22	2	9	11	1	<10	31	10

The MgZr substrates were cut from the ingots using a diamond wire saw of 150 µm at 0.8 rpm under ethanol as lubricant. Polishing steps were performed using SiC paper of different grades (500 then 1200) using diamond suspensions of 9 and 3 µm on clothes (MD-Largo and MD-Dac) with lubricant and ethanol. Final polishing was achieved using vibrational polishing with a 40 nm colloidal silica solution mixed with 50 vol.% of ethanol on MD-NAP (Struers, France). Afterwards, the MgZr samples were cleaned in ethanol for 15 min in an ultrasonic bath, rinsed with ethanol, dried under Ar, and saved in a N_2 glove box to avoid potential oxidation before embedding in the geopolymer.

The geopolymers $1Na_2O–3.96SiO_2–1Al_2O_3–12.5H_2O$ with or without NaF, GP, and NaF-GP, respectively, were prepared as reported in our previous study [17]. This composition corresponds to the model geopolymer used as a reference in most of scientific studies [2,19,22] and for MgZr encapsulation. The activation solution prepared by the dissolution of 16.92 g of sodium hydroxide (NaOH pellets, Sigma-Aldrich, Molsheim, France, purity 99.9%,) in 130.04 g of commercial sodium silicate solution, the Betol 39T (Woellner, Germany, composed of 27.80 wt% of SiO_2, 8.30 wt% of Na_2O, and 63.90 wt% of H_2O) was mixed with 3.68 mL of ultrapure water under magnetic stirring during one hour. Due to the exothermic reaction of silicate dissolution, the activation solution was cooled down to room temperature during the mixing. Afterwards, 102.44 g of metakaolin (Argical-M-1000 from AGS Mineraux, Clérac, France, composed of 54.40 wt% of SiO_2, 38.40 wt% of Al_2O_3, and 7.2 wt% of impurities) was added to the activation solution and stirred

during 10 min until the solution homogenization. NaF-GP was prepared by a simple addition of sodium fluoride (NaF, 99%, Strems Materials Bischheim, France) solution at 1.25 M (0.012 wt%) to the activation solution and the solution was stirred during 1 h before the metakaolin addition. For information, the composition of the poral solutions extracted from these geopolymers also reported in [17] are presented in Table 2.

Table 2. Geopolymers, pH, and composition of the solutions used in this study.

Geopolymer	pH	[Na] mmol.L^{-1}	[Si] mmol.L^{-1}	[F] mmol.L^{-1}	[Cl] mmol.L^{-1}
GP	12.37	418.9 ± 6.5	46.6 ± 15.8	19.0 ± 0.4	27.4 ± 0.5
NaF-GP	12.40	1116.5 ± 237.8	32.9 ± 9.1	1855.9 ± 37.1	20.0 ± 0.4

2.2. Sample Preparation

The MgZr substrates were placed in polytetrafluoroethylene holders and covered with geopolymer just after its preparation, when the geopolymer was still viscous. The two sets were prepared, including or excluding the NaF additive, and are referred hereafter as GP-NaF and GP, respectively. The samples were then placed in a desiccator containing a saturated solution of KCl, fixing a relative humidity (RH) of 82% at 25 °C [23] during 90 days to avoid the drying of the geopolymer. A typical sample is shown in Figure 1.

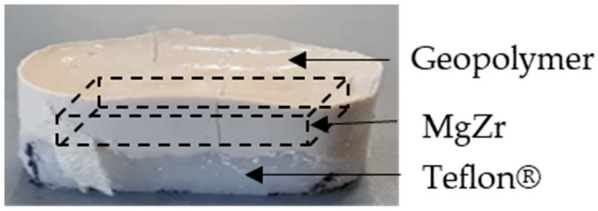

Figure 1. Description of a sample.

After the in situ characterization described below, the two samples were frozen and freeze-dried during 24 h with a LABCONO FreeZone 2.5 Freeze Dry System (Kansas, Mo, USA). This method preserves the material porosity and minimizes the crack [24]. Afterwards, cross-sections and thin foils (about 200 nm thick) of the geopolymer/MgZr samples were prepared.

2.3. Characterization

Samples GP and GP-NaF were characterized using Grazing Incidence hard X-Ray Diffraction (GI-XRD) at 27 keV (λ = 0.4592 Å) on BM32 beamline at the European Synchrotron Radiation Facilities (Grenoble, France). Hard X-rays were required to cross the geopolymer, and then to probe the CP formed at the surface of MgZr. To analyze various depths in the MgZr substrate, the incident angle of the beam was fixed at α_i = 0.1 and 0.5°. In a first approximation, considering that the surface mainly consists in $Mg(OH)_2$ and Mg, the penetration depth was assessed between 10 µm at 0.1° and a few ten of microns at 0.5° (see Figure S1). Data were acquired between 1 and 31° during 25 min with a 0.01° step. For easy understanding, GI-XRD patterns are presented as a function of d-spacing (Å) ($d = \frac{\lambda}{2\sin\theta}$).

Raman microspectroscopy was used to characterize CP layer from samples prepared as cross-sections. Raman measurements were carried out in backscattering geometry configuration, on a Horiba Jobin Yvon LabRAM Aramis confocal Raman microscope (France) at the Institut de Chimie Séparative (Marcoule, France), using an excitation wavelength of λ = 532 nm with a laser spot size of about 1 mm with an objective of ×100 working distance. The analysis was performed by the embedding resin, which results in several peaks between 1000 and 3400 cm^{-1}. Thus, Raman data were recorded between 3600 and 3700 cm^{-1} to characterize the presence of Mg–O–H Ag1 peaks of brucite ($Mg(OH)_2$) structure.

Cross-sections of samples were also analyzed by Scanning Electron Microscopy (SEM) with an FEI Quanta 200 environmental scanning electron microscope (Hillsboro, OR, USA) using a back-scattered electron detector (BSED) or a secondary electron detector (SED) in vacuum conditions with an acceleration voltage of 5 kV to avoid a degradation of the material at the Institut de Chimie Séparative (Marcoule, France). Energy-dispersive X-ray spectroscopy (EDX) elemental mapping was performed during 20 min with an energy of 1 keV. The average thickness of CP layers was measured from SEM images on the whole length of the cross-section using the Fiji software to take into account the local variation of the CP layer thickness.

Thin foils for electron microscopy were prepared with a dual-beam FIB using FEI Helios 600,192 NanoLab at the Centre Pluridisciplinaire de Microscopie Electronique et de Microanalyse (Marseille, France). Analyses by Scanning Transmission Electron Microscopy (STEM) were carried out using a JEM ARM 200F (JEOL) transmission electron microscope equipped with a cold-field emission gun and a CEOS aberration corrector of the objective lens [25] at the Laboratoire des Matériaux et Phénomènes Quantiques (Paris, France). Careful attention was paid to the choice of the observation conditions in order to limit sample damage. Indeed, oxide and hydroxide can be damaged by the electron beam at high voltage [26,27]. Thus, we set the TEM voltage to 80 kV. Sample imaging and spatially resolved elemental analysis at the nanoscale were undertaken in scanning TEM mode using high Annular Angle Dark Field (HAADF) imaging and EDX spectroscopy, respectively. A spot size XC was used with a half convergence angle of 16 mrad for both imaging and spectroscopy. HAADF-STEM images were acquired with inner and outer collection angles of 90 and 370 mrad, respectively. EDX spectra were collected on 300 × 300 nm^2 area during 45 s with an EX-24063 JGT detector. Spatial distributions of elements (Si, Al, Mg, O, F, Na) were determined by integrating the peak area after a background subtraction. The porosity and the mean pore size of the CP layers were extracted from STEM images using binary images with the "trainable WEKA segmentation" and "analyse particles" plug-ins of the Fiji software (version 2). The analysis was performed on 2 different areas of the CP layer and repeated 4 times to reduce the random user error. The protocol of image processing is presented in Supplementary Materials.

3. Results

3.1. Nature of CP

3.1.1. In Situ GI-XRD

The GI-XRD patterns at α_i = 0.1 and 0.5° of GP and GP-NaF are presented in Figure 2a,b.

As is visible by the GI-XRD patterns, some intense peaks corresponding to the Mg hexagonal phase (ICDD-JCPDS card No. 01-082-9643) are visible but some peak extinctions and/or peak intensity variation with α_i can be observed. As examples, the peak at 1.90 Å is not present for the sample GP (Figure 2a) and the peak at 1.46 Å for the sample GP-NaF increases with α_i. These results can be explained by, first, the existence of various crystallographic grain orientations within the MgZr alloy as shown by the patterns obtained from XRD of several MgZr substrates performed with various orientations (Figure S2). This can be caused by several phenomena: (i) the inhomogenous inclusions of Zr within the alloy [28], (ii) the Zr inclusions limiting the grains growth during the manufacturing process [29], and/or (iii) the preparation of the alloy bare including extrusion and drawing steps. Second, the substrate preparation, cutting and polishing, can induce twining formation [30]. This leads to the formation of new crystalline orientations.

Low intensity peaks attributed to several CP can also be observed. This low intensity may be due to a low amount and/or crystallinity of CP and also by the rough interface existing between MgZr and CP layer. Whatever the samples, without or with NaF, GI-XRD patterns present some peaks which may be attributed to magnesium silicates such as $MgSiO_3$ (orhtoenstatite, ruff No.R040093) and Mg_2SiO_4 (Forsterite, ruff No. R040057). $Mg(OH)_2$ (Brucite, ICDD-JCPDS card No. 01-071-5972) is also observed but mostly at

large incidence (i.e., in deeper in the sample). Patterns of the GP-NaF sample show supplementary peaks of $NaMgF_3$ (Neighborite, ICDD-JCPDS card No. 01-070-3874).

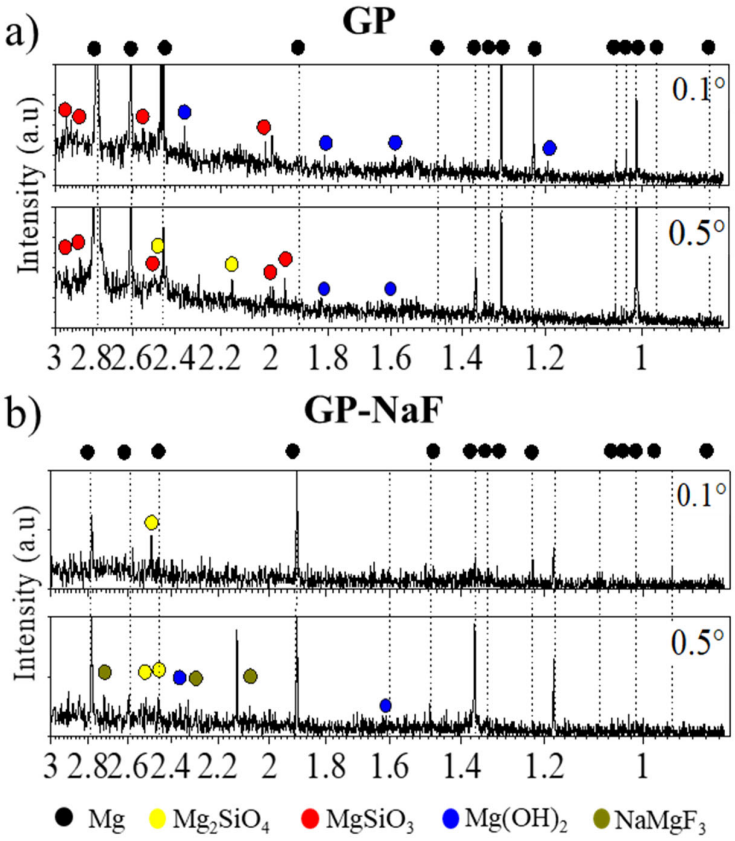

Figure 2. Grazing Incidence hard X-ray Diffraction (GI-XRD) patterns obtained at different incidences angles α_i = 0.1 and 0.5° of (**a**) GP and (**b**) GP-NaF.

3.1.2. Raman Microspectroscopy

Local analyses presented in Figure 3 were performed on two zones of the CP layers for each sample.

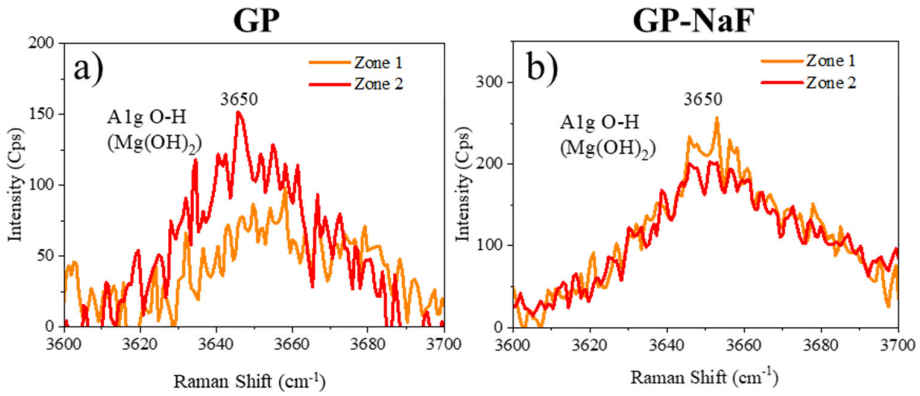

Figure 3. Raman spectra of 2 zones of the corrosion product (CP) layers of samples (**a**) GP and (**b**) GP-NaF.

GP and GP-NaF spectra presented in Figure 3 confirm the presence of Brucite highlighted by GI-XRD, showing a broad peak at 3650 cm^{-1} corresponding to the $A1_gO$-H stretching mode in $Mg(OH)_2$ crystals [31]. The large peak width attests of a low crystallinity of $Mg(OH)_2$.

3.2. Morphology and Composition of the Interfaces

Images of the sample cross-sections and their relative EDX elemental mapping obtained from SEM-EDX are presented in Figure 4.

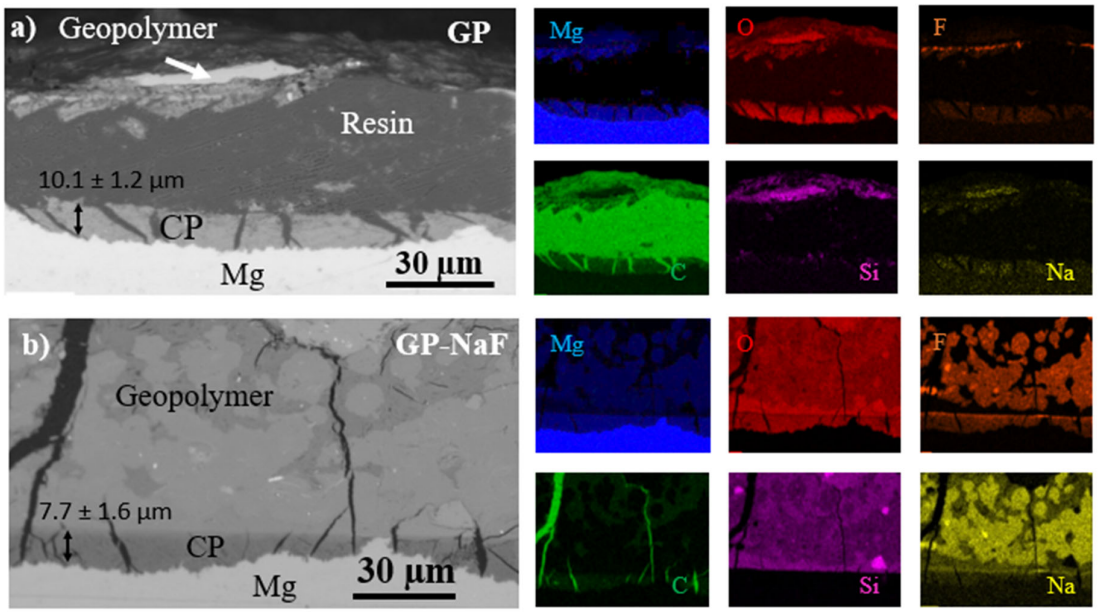

Figure 4. BSED-SEM images and EDX cartographies of Mg, O, F, C, Si, and Na of (**a**) GP and (**b**) GP-NaF.

These results highlight the presence of cracks perpendicular to the surface of the MgZr substrate in the CP layers and geopolymers for all samples. For GP (Figure 4a), a delamination of the geopolymer from the CP film is noticeable. Indeed, during the geopolymer ageing, cracks and delamination can be formed due to the shrinkage of the geopolymer occurring during the geopolymerization [19] and to a lesser extent during the sample preparation (freezing step) [32,33]. Moreover, the production of hydrogen during the MgZr corrosion may lead to a partial rupture of the CP and/or to CP expansion [12].

The average thickness of CP layers, determined as described in Materials and Methods section, is lower for sample with NaF (7.7 $\pm$ 1.6 µm) than for sample without NaF (10.1 $\pm$ 1.2 µm).

Regarding the composition of the CP layer, the EDX mapping presented in Figure 4 reveals the presence of Mg, O, and F for all samples. For a sample without NaF, the composition of the CP layer is homogenous. A slight amount of F is detected due to the F impurity inside the poral solution [2] which diffuses through the CP layer, as it has been reported from the characterization of CP layers formed during the corrosion of MgZr substrate in poral solution extracted from geopolymer [17]. The CP layer from the GP-NaF sample is not homogenous and shows an enrichment in F and Na at the surface of the CP layer in contact with the geopolymer.

All of these results are consistent with the GI-XRD data, revealing the existence of $Mg(OH)_2$ and of magnesium fluoride such as $NaMgF_3$ for GP-NaF. However, magnesium silicates are not detected in the CP layer.

An enrichment of Mg in the geopolymer where Si, O, and Na are detected is also revealed for both samples. The presence of Mg was also confirmed by the local EDX analysis performed at a distance of 5 µm from the CP layer (Figure 5). The diffusion of Mg in the poral solution of the geopolymer during MgZr corrosion and/or the partial dissolution of CP such as $Mg(OH)_2$ may explain this enrichment. This would change the composition of the poral solution and lead to the formation of magnesium silicates in the GP zone close to the CP layer as characterized by GI-XRD.

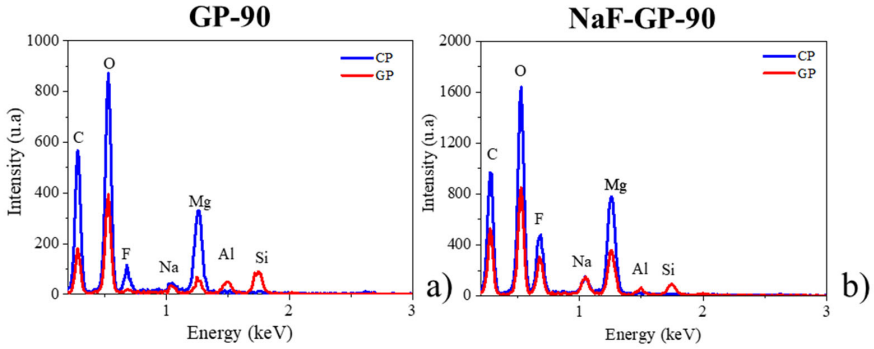

Figure 5. EDX spectra measured in CP at a distance of 5 µm from the CP layer for (**a**) GP and (**b**) GP-NaF samples.

For the sample GP-NaF, some areas are mainly composed of Na and F coming from the precipitation of NaF during the geopolymerization process and/or from the formation of compounds reacting during geopolymerization steps such as Na_2SiF_6 or Na_3AlF_6 [19]. These species act as a F reservoir that can react with dissolved Mg. The EDX analyses also highlight that F is not homogenously distributed in the geopolymer.

3.3. Characterisation at the Nanoscale

Morphology and Composition of CP

To study the morphology and the composition of CP layers at a nanoscale, thin foils of the GP and GP-NaF samples were analyzed using STEM-EDX. Figure 6 presents HAADF STEM images of zones located around the MgZr/CP interface and elementary profiles of a GP thin foil and a GP-NaF thin foil, respectively. For the GP sample, the CP layer making up a large part of the thin foil, only part of it has been analyzed.

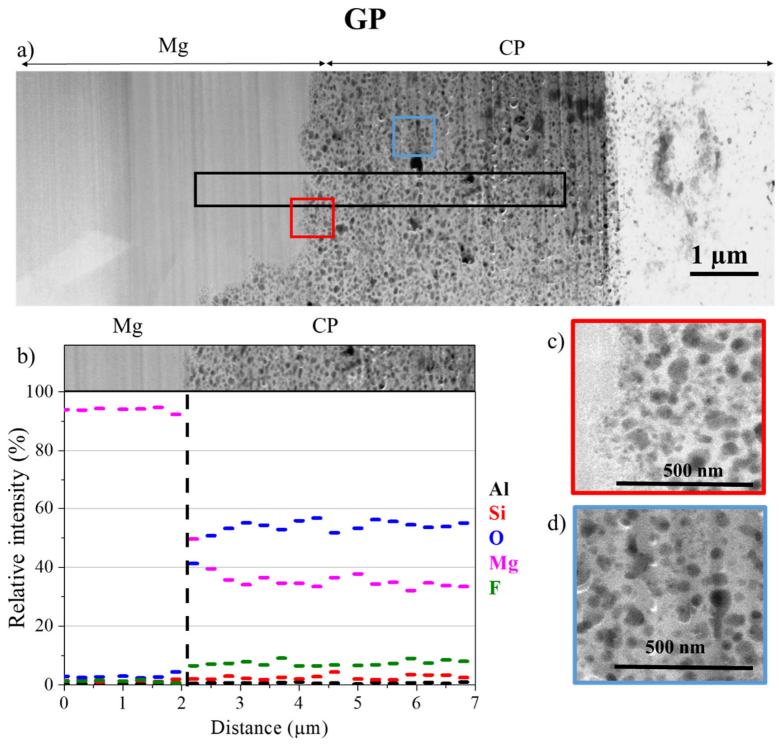

Figure 6. (**a**) Low magnification of HAADF-STEM images assembly of the interface between CP, MgZr for GP thin foil, (**b**) spatial distributions of elements obtained from EDX analysis (black rectangle in (**a**)), zooms of the square areas enclosed in (**c**) red and (**d**) blue in (**a**). The difference in STEM contrast in the CP layer is due to a difference of thin foil thickness.

For the GP sample (Figure 6), the analyzed area of the CP layer is homogenous, porous, and mainly consists of Mg and O with few amounts of F and Si (Figure 5b). The presence of these elements may attests of the formation of $Mg(OH)_{2-x}F_x$ ($x << 1$). The Brucite partially substituted by F may present a semi-crystalline structure as characterized by Raman microspectroscopy and GI-XRD.

For the GP-NaF sample, the thickness of the CP layer measured from the STEM image of 6.4 µm (Figure 7a) is about the same order of magnitude than the one obtained from SEM image analysis. The CP layer presents several zones highlighted in Figure 7b.

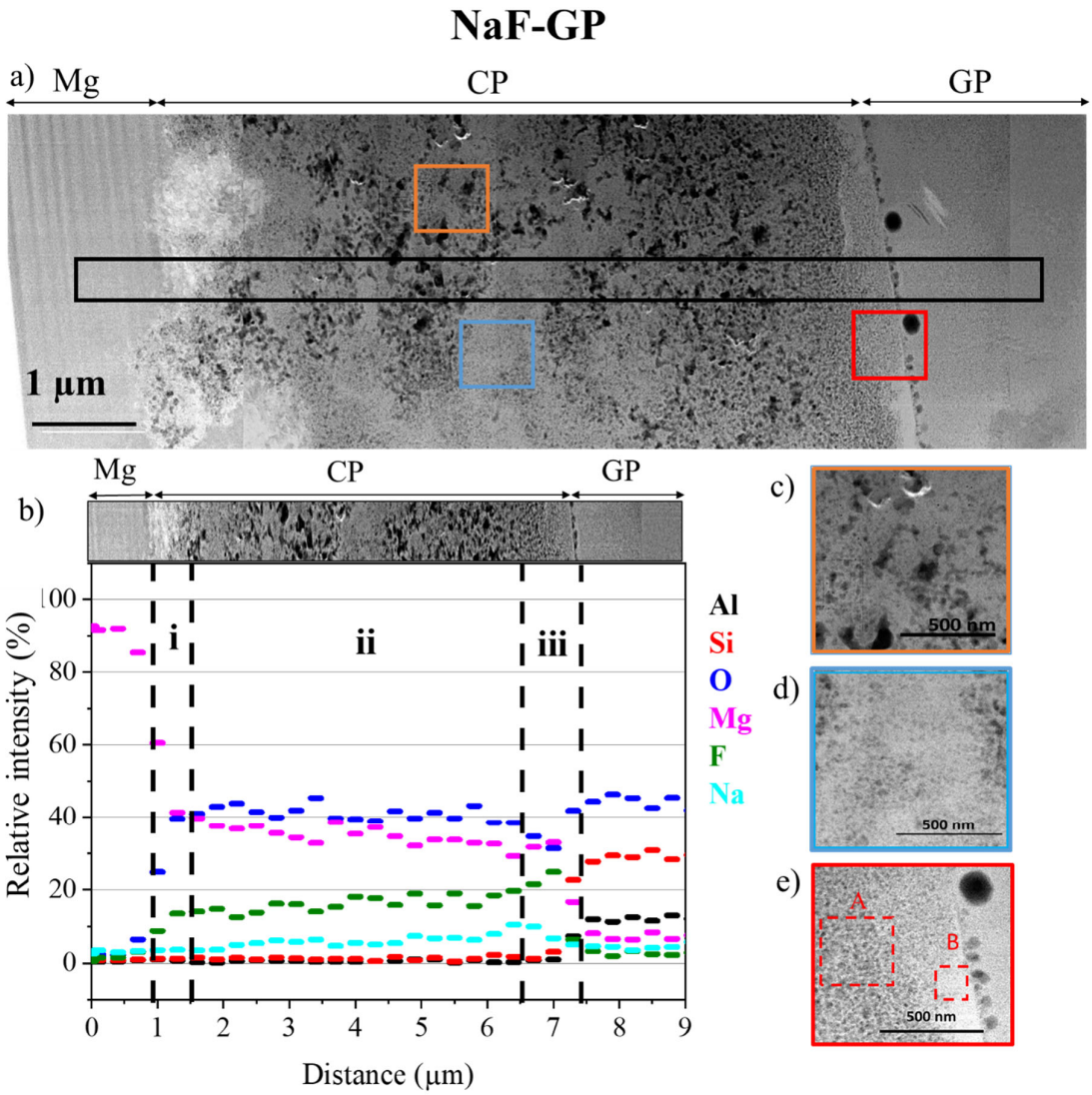

Figure 7. (**a**) Low magnification of HAADF-STEM images assembly of the interface between CP, MgZr for GP-NaF thin foil, (**b**) spatial distributions of elements obtained from EDX analysis (black rectangle in (**a**), zooms of the square areas enclosed in (**c**) red, (**d**) blue, and (**e**) orange in (**a**).

The first zone (i) which is 600 nm-large is located at the surface of MgZr. This zone is dense and mainly consists of Mg, O, and F. This composition may correspond to a mixture of MgZr and $Mg(OH)_{2-x}F_x$ as reported in [27,34]. The second porous zone (ii) is 5.4 µm large and is a mix of two sets of porous texture. In this zone, the presence of Mg, O, and of a gradient of Na and F may indicate the formation of $Mg(OH)_{2-x}F_x$ ($x \geq 1$) and $NaMgF_3$ phases [9]. The two sets of porous texture may be attributed to these two phases as displayed in Figure 7c,d. The last zone of 450 nm close to the GP (iii) is denser than the zone (ii) as attested by the presence of clear area in Figure 7e (zone B) in contact with the CP-GP interface. This goes with an increase of F that may lead to a densification of the CP

layer either by the formation of highly substituted $Mg(OH)_{2-x}F_x$ and the high amount of $NaMgF_3$. These results are consistent with GI-XRD analyses.

As observed by SEM-EDX, Mg has diffused into the GP-NaF during the MgZr corrosion. Here too, the magnesium silicates characterized by GI-XRD can be formed into the pores of the geopolymer. Moreover, some holes having the morphology of bubbles are located at the interface between the CP layer and the geopolymer. These "bubbles" may come from the H_2 release due to the corrosion of MgZr. This shape preservation probably means that high H_2 production occurs at the first time early after the contact of the MgZr substrate with the geopolymer, i.e., before the end of the geopolymer stiffening (3 to 4 h) [35].

3.4. Porosity of CP Layer

The porous texture evolution of the CP layers is an important characteristic for the long-term behavior of the waste materials, since it drives the H_2 diffusion and then its release in the media. Thus, HAADF STEM images of the various zones of the CP layers were treated with the following procedure illustrated in Figure 8 using the Fiji software. First, the scale bar from the raw image was linked to the pixel of the image. Second, after a smoothing process on image 1, Trainable Weka Segmentation was applied to generate image 2 by selecting two zones: one for pores (holes) and one for solid. Third, binary image 3 was then obtained by applying a threshold to image 2. Finally, porosity, pore size distributions, the number of particles analyzed, and their size in μm^2 were obtained from image 3 using the "Analyse Particles" function. To reduce the user error, this protocol was applied four times on each image. In addition, two different images were taken on each sample to have a better statistic.

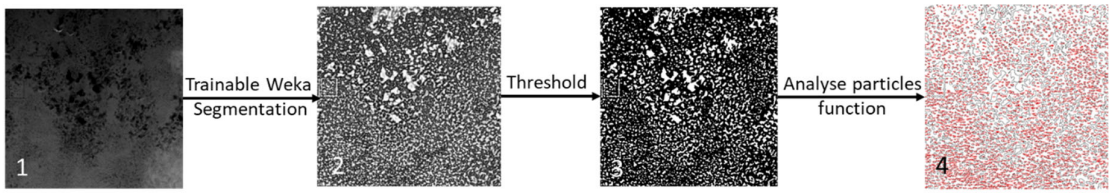

Figure 8. Protocol of image processing for the porous texture analysis of the CP layers.

The dataset obtained from the image analysis with the protocol presented previously was used to perform statistical analysis of pore size distribution considering that images of the pores have disk shapes. Figures 9 and 10 present the disk (pore) size distribution of GP and NaF-GP, respectively, and the Table 3 the porosity, the mean, and the median pore size obtained with this procedure. The totality of the results obtained by statistical analysis of the dataset from image analysis can be found in Supplementary Materials (Table S1).

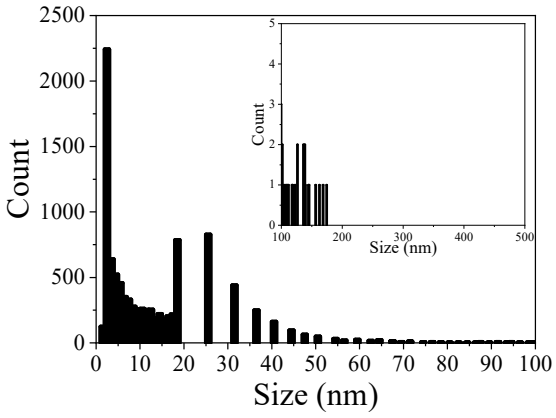

Figure 9. Histogram of the disk size distribution of GP.

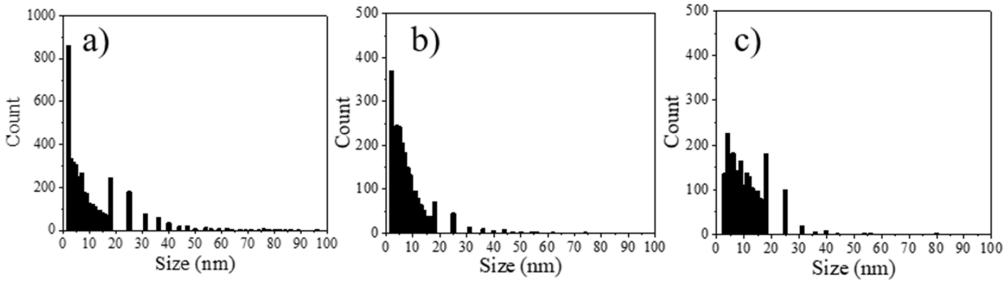

Figure 10. Histograms of the disk size distributions of GP-NaF for (**a**) image (c), (**b**) image (d), and (**c**) image (e) from Figure 7.

Table 3. Porosity, mean, and median pore size in CP layers of samples obtained by STEM images analysis using the Fiji software.

Sample	Zone	Porosity (%)	Mean Pore Size (nm)	Median Pore Size (nm)
GP (Figure 6)	CP layer	38.2 ± 5.9	13.6	8.5
GP-NaF (Figure 7)	Orange square—image (c)	28.9 ± 0.7	10.5	6.5
	Blue square—image (d)	22.5 ± 2.5	7.9	6.1
	Red square—image (e)	21.2 ± 1.8	10.8	9.7
	zone A	Not measureable	Not measurable	Not measurable
	zone B			

The porosity of the CP layers presented in Table 3 are between 40% and 60% lower than the one reported for $Mg(OH)_2$ in the literature [34,36]. Moreover, these results show that the CP porosity and the pore size in the GP-NaF sample are smaller than those in the GP sample. The analysis of the CP pore size distributions reveal that more than 75% of the CP pores are smaller than 14.4 nm for the GP-NaF sample and 17.8 nm for the GP sample (Figures 9 and 10).

Additionally, the CP porosity in the GP-NaF sample decreases closer to the CP-GP interface. Moreover, zones (ii) and (iii) present a mix of porous texture. The presence of porous texture (28.9% and 22.5% for zone (ii), and 21.2% porosity and dense solid for zone (iii)) may be associated to two phases, $Mg(OH)_{2-x}F_x$ and $NaMgF_3$, and/or to a non-uniform densification of $Mg(OH)_{2-x}F_x$ due to the isomorphic substitution of OH by F [21,37].

4. Discussion

The multiscale characterizations of the CP layers formed in geopolymer without and with NaF have shown the formation of various CP layers having different morphology and composition. The processes at the origin of the formation of these CP are summarized in Figure 11.

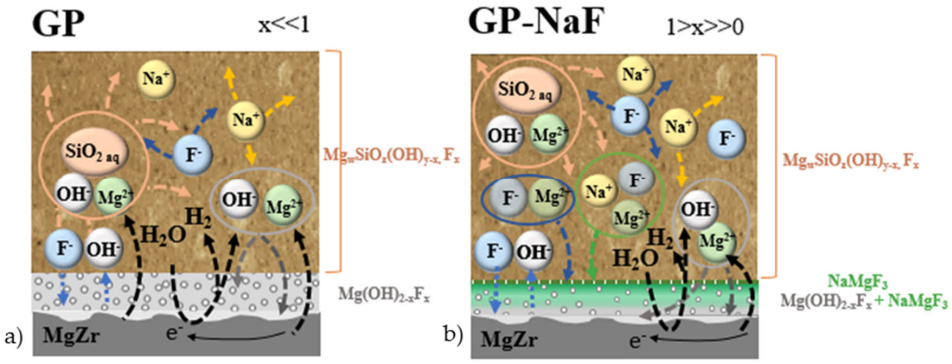

Figure 11. Diagram summarizing the processes which can possibly occur during 3 months of MgZr alloy corrosion in (**a**) GP and (**b**) GP-NaF.

4.1. General Description of the Samples

In all samples, the CP layer mainly consists of an amorphous/lowly crystalline $Mg(OH)_2$ structure. Brucite formation is classically characterized in solution at pH > 10.5 [38] after the local dissolution of magnesium following Equation (1).

$$Mg^{2+} + 2\ OH^- \rightarrow Mg(OH), \quad (1)$$

because F^- is present in poral solution of the geopolymer, the Brucite is partially substituted by an isomorphic exchange of the OH groups by F forming $Mg(OH)_{2-x,}F_x$ (2).

$$Mg(OH)_2 + xF^- \rightarrow Mg(OH)_{2-x,}F_x + xOH^-, \quad (2)$$

with x << 1 when the MgZr corrosion occurred in GP and x >> 0 in GP-NaF.

For the CP layer formed in GP-NaF, $NaMgF_3$ is also present and its concentration increases with the distance from the MgZr/CP interface. The presence of $NaMgF_3$ in the CP layer can be explained by the high concentration of F^- in the poral solution of the geopolymer in contact with the MgZr alloy. This high concentration allows the complete substitution of OH groups by F leading to the formation of MgF_2, and then, the precipitation of $NaMgF_3$. This phenomenon has been already characterized with nanospheres of MgF_2 reacting with NaF at high concentration (3) to form $NaMgF_3$ [39].

$$MgF_2 + NaF \rightarrow NaMgF_3. \quad (3)$$

For both samples, magnesium silicates such as $Mg_wSiO_z(OH)_{y-x}F_x$ (with x << 1 in GP and x >> 0 in NaF-GP) are not observed in the CP layer, and thus, are probably localized within the geopolymers. This result is different from the one obtained during the MgZr corrosion in poral solutions extracted from the geopolymers used in this study [17] but probably similar to the ones obtained in the work of Barros et al., as they have detected the presence of magnesium within the geopolymer [21]. To form magnesium silicates, dissolved magnesium diffuses through the CP layer to the poral solution of the geopolymer, reacts with silicates species present in solution, and precipitates. Such a phenomenon particularly favored in nanoconfinement can lead to a pore clogging already observed in model systems [40,41], during glass alteration [42–44], but also in geopolymer during ageing time [2]. This may limit the transport of the poral solution to the surfaces of the CP and MgZr.

4.2. Origin of the Porous Texture

Depending on the presence of NaF within the geopolymer, the porosity and the pore size distribution of the CP layers are different. Two phenomena can explain these various porous textures.

First, the substitution of OH groups of Brucite by F decreases the cell volume of $Mg(OH)_{2-x}F_x$, as it is reported in the humite system (from the $MgO\text{-}SiO_2\text{-}H_2O$ compounds) [37] and may lead to a possible densification of the $Mg(OH)_{2-x,}F_x$ when x increases [12]. Thus, an increase of the F concentration in the media should go with an increase of the $Mg(OH)_{2-x}F_x$ densification which is the case of the CP layers formed in the GP-NaF sample. Moreover, several studies have showed that an increase of x allows a better stability of $Mg(OH)_{2-x,}F_x$ in solution regarding its dissolution [45,46].

Second, when F is present within the geopolymer, the formation of two phases within the CP layer may also decrease the porosity. Indeed, when Brucite is formed at the interface MgZr/CP layer, Na and F may diffuse within the porosity, forming $Mg(OH)_{2-x,}F_x$ and then $NaMgF_3$ following (1) and (3). Moreover, the high amount of $NaMgF_3$ in the top zone of the CP layer of the GP−NaF sample is associated with a low porosity. This means that $NaMgF_3$ precipitation may limit the transport of poral solution and Mg^{2+}.

4.3. Relation between the Porous Texture and the Protective Properties of the CP Layer

The results obtained in this study have shown that the CP layers formed in GP-NaF is thinner than the CP layer formed in GP sample, 7.7 ± 1.6 µm vs. 10.1 ± 1.2 µm. In these experiments, it is not possible to rigorously compare the MgZr corrosion from the CP layer thickness since the CP formation is not isovolumic regarding MgZr corrosion. The volume occupied by the phases depends mainly on their crystalline structures and CP can undergo dissolution/precipitation processes.

However, taking into account, both the porous texture and the thickness, it is possible to assess the protective properties of the CP layers regarding MgZr corrosion. The CP layer formed in GP-NaF presents a lower porosity and thickness than the CP layer formed in GP, and thus it is probably more protective. These protective properties are associated with, first, the porous texture driving the solution and Mg^{2+} transport through the CP layer and, second, with the phases stability regarding their dissolution. NaF in solution allows the densification of the CP layer by the increase of x in $Mg(OH)_{2-x,}F_x$ and the formation of $NaMgF_3$ and the enhancement of the stability of $Mg(OH)_{2-x,}F_x$ in solution [45,46]. These results are also in good agreement with several works performed by electrochemical analysis in a similar system [18–20] adding NaF as corrosion inhibitor inside a geopolymer.

4.4. Comparison with the CP Layers Formed in Poral Solution Extracted from Geopolymer

In our previous study [17], we investigated the evolution of the CP layers formed during the corrosion of MgZr in poral solutions extracted from the same geopolymers with and without NaF used in the present study. Comparing those results, two main differences between the CP layers formed in poral solution and within geopolymer can be noted.

First, in poral solutions, magnesium silicates form within the CP layer, while in geopolymer, the magnesium silicates precipitation occurs mainly within the geopolymer pore network. This highlights that dissolved silicates diffused probably more slowly than F and Na through the geopolymer and to the CP layer. The size of the silicate species, the low solubility of the magnesium silicates, and/or their interactions with CP pore surface may be at the origin of this precipitation within the pores of the geopolymer. Such precipitation may lead to a pore clogging.

Second, with or without corrosion inhibitor, the size of the CP layers formed in poral solutions are lower than the one formed within the geopolymers. Once again, even if the MgZr corrosion cannot be quantified, it is possible to assume that MgZr corrosion is higher in geopolymer than in poral solution. This corrosion difference is mainly due to the amount and the availability of dissolved species present in solution in contact with the MgZr alloy surface that drives the nature of CP formed and probably their protective properties. In corrosion experiments performed with poral solutions, the numerous solution renewals allow the supplying of SiO_2 (aq) and F^- species participating to the formation of a protective CP layer consisting of magnesium silicates and fluorine phases ($Mg(OH)_{2-x,}F_x$ and $NaMgF_3$). In the geopolymer, these dissolved species are not directly available on the total surface of MgZr as illustrated by the F and Na distributions in geopolymer presented on SEM-EDX cartographies in Figure 4. This may lead to the formation of less protective CP layers.

The transport and the discharge of hydrogen formed during MgZr corrosion in geopolymer is different from the one in the solution. In the solution, hydrogen can be released in the atmosphere above the solution while in geopolymer, its production can lead to a repulsion of the poral solution. This may result in a decrease of the MgZr corrosion and in phase precipitation within the pores of the geopolymer.

4.5. Proposition of Interconnected Processes

Combining the results of this study with those obtained previously from the study of the MgZr corrosion in poral solution [17], a diagram taking into account the processes and their interconnections involving during the corrosion of MgZr alloy within geopolymer is proposed in Figure 12.

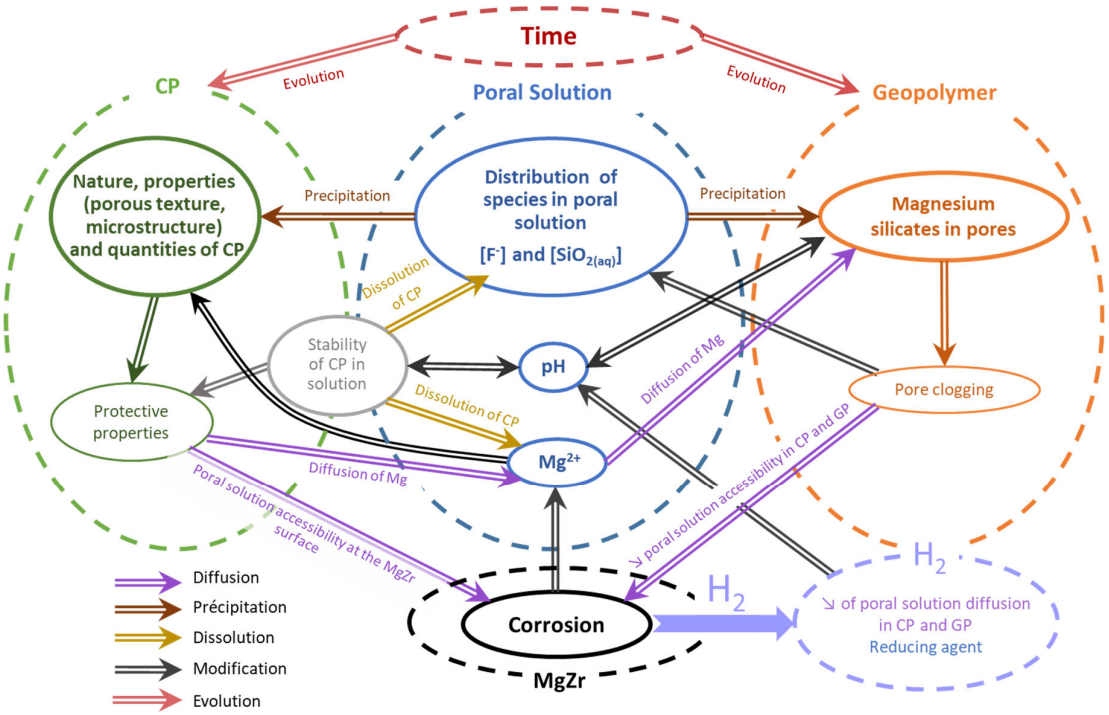

Figure 12. Proposition of interconnected processes involving during the corrosion of MgZr within geopolymers.

When the MgZr alloy is embedded in a geopolymer, the poral solution in contact with the MgZr surface corrodes the alloy that leads to the formation of Mg^{2+} and H_2. At the pH of the poral solution, dissolved magnesium reacts to form CP such as $Mg(OH)_{2-x},F_x$ and $NaMgF_3$ when the F^- amount is high enough within the media. The reactive diffusion of Mg^{2+} to the poral solution of the geopolymer leads to magnesium silicates precipitation within the pores and may lead to a pore clogging. The formation of protective CP layer that increases with F concentration in poral solution, and magnesium silicates limits the access of the poral solution to the MgZr surface. This process is self-limited in time since the Mg^{2+} supply decreases with the increase of the CP layer protective properties and magnesium silicates precipitation. The consequences of these phenomena, CP formation, magnesium silicates precipitation, and H_2 formation, may modify the original pH. This modification can change the stability of the CP and leads to their dissolution and then a decrease of their protective properties and a possible resumption of MgZr corrosion.

The last important parameter affecting the evolution of this system is the time. Indeed, CP, geopolymers, magnesium silicates are metastable phases, at least the ones characterized here. With time, it is expected that they become more crystallized. Such crystallization will change their porous texture which will have consequences on the protective properties of the CP layer, the reactive diffusion of the poral solution within the geopolymer, and the H_2 release in geological disposal.

5. Conclusions

In this study, combining in situ and ex situ characterizations and a multiscale approach, we have analyzed the composition, the morphology, and the porous texture of the corrosion products and evidenced the effect of the corrosion inhibitor NaF during the corrosion of MgZr embedded in geopolymer. We determined the formation of $Mg(OH)_{2-x}F_x$, x increasing with the amount of F species within the geopolymer. In addition, in presence of NaF, $NaMgF_3$ forms leading to a decrease of the thickness and the porosity of the corrosion products layer. Moreover, the precipitation of magnesium silicates within the porosity of the geopolymer was highlighted. Finally, combining the results of our previous study,

we have proposed a set of interconnected processes occurring during the MgZr corrosion in geopolymer.

Even if these processes are well identified, two factors which can modify them have to be studied in perspective. The first one is the effect of the irradiation due to the radionuclides traces remaining at the surface of the fuel cladding after the spent nuclear fuel removal. Indeed, the irradiation occurring during the corrosion as well as their effect on the geopolymer matrix may modify the evolution of the system. Today, several experiments are ongoing to precisely characterize this effect. The second one is the effect of long timescale. The prediction of the long-term corrosion of MgZr alloy is required to be able to calculate the amount of hydrogen release in the geological disposal. This calculation can only be determined using modelling since the available experiments are performed at a laboratory time scale. Such predictive modelling can be enhanced by the study of natural and archaeological analogous system.

Supplementary Materials: The following are available online at https://www.mdpi.com/article/10.3390/ma14082017/s1, Figure S1: Penetration depth of the X-ray beam at 27 keV at a function of the incident angles, Figure S2: XRD patterns of two MgZr substrates analyzed in different position. Table S1: Summary of the results obtained by statistical analysis of dataset from image analysis.

Author Contributions: R.B.: conceptualization, investigation, writing, original draft preparation. J.N.: STEM-EDX analysis, S.T.: formal analysis, X.D.: formal analysis, review & editing, D.R.: conceptualization, writing, original draft preparation. All authors have read and agreed to the published version of the manuscript.

Funding: This research was performed within the investments for the future program of the French Government and operated by the French National Radioactive Waste Management Agency (Andra).

Institutional Review Board Statement: Not applicable.

Informed Consent Statement: Not applicable.

Data Availability Statement: Not applicable.

Acknowledgments: The authors acknowledge financial support from the CNRS-CEA "METSA" French network (FR CNRS 3507) (METSA, 2019) for the STEM experiments conducted on the MPQ (Université Paris Diderot) platform. The authors gratefully acknowledge B. Muzeau from LECBA at CEA Saclay and M. Le Flem from LECA at CEA Saclay for letting us use their labs for MgZr samples preparation and MgZr supply. François Rieutord is also acknowledged for his help on ESRF experiments.

Conflicts of Interest: The authors declare no conflict of interest.

References

1. Caillat, R.; Hérenguel, J.; Salesse, M.; Stohr, J. Raisons du choix de l'alliage Mg-Zr pour le gainage des elements combustibles. *J. Nucl. Mater.* **1963**, *8*, 1–2. [CrossRef]
2. Benavent, V.; Frizon, F.; Poulesquen, A. Effect of composition and aging on the porous structure of metakaolin-based geopolymers. *J. Appl. Cryst.* **2016**, *49*, 2116–2128. [CrossRef]
3. Duxson, P.; Fernández-Jiménez, A.; Provis, J.L.; Lukey, G.C.; Palomo, A.; Van Deventer, J.S.J. Geopolymer technology: The current state of the art. *J. Mater. Sci.* **2007**, *42*, 2917–2933. [CrossRef]
4. Davidovits, J. *Geopolymer Chemistry and Applications*; Institut Géopolymère: Saint-Quentin, France, 2011; ISBN 9782954453118.
5. Perera, D.S.; Blackford, M.G.; Vance, E.R.; Hanna, J.V.; Finnie, K.S.; Nicholson, C.L. Geopolymers for the Immobilization of Radioactive Waste. *MRS Proc.* **2004**, *824*, CC8.35. [CrossRef]
6. Jantzen, C.M.; Lee, W.E.; Ojovan, M.I. Radioactive waste (RAW) conditioning, immobilization, and encapsulation processes and technologies: Overview and advances. In *Radioactive Waste Management and Contaminated Site Clean-Up: Processes, Technologies and International Experience*; Savannah River Site (S.C.): Aiken, SC, USA, 2013; pp. 171–272. ISBN 9780857094353.
7. Van Jaarsveld, J.G.S.; Van Deventer, J.S.J.; Lorenzen, L. The potential use of geopolymeric materials to immobilise toxic metals: Part I. Theory and applications. *Miner. Eng.* **1997**, *10*, 659–669. [CrossRef]
8. Li, Q.; Sun, Z.; Tao, D.; Xu, Y.; Li, P.; Cui, H.; Zhai, J. Immobilization of simulated radionuclide 133Cs+ by fly ash-based geopolymer. *J. Hazard. Mater.* **2013**, *262*, 325–331. [CrossRef] [PubMed]
9. Liu, X.; Ding, Y.; Lu, X. Immobilization of simulated radionuclide 90Sr by fly ash-slag-metakaolin-based geopolymer. *Nucl. Technol.* **2017**, *198*, 64–69. [CrossRef]

10. Cantarel, V.; Nouaille, F.; Rooses, A.; Lambertin, D.; Poulesquen, A.; Frizon, F. Solidification/stabilisation of liquid oil waste in metakaolin-based geopolymer. *J. Nucl. Mater.* **2015**, *464*, 16–19. [CrossRef]
11. Perrault, G.G. The potential-pH diagram of the magnesium-water system. *J. Electroanal. Chem. Interfacial Electrochem.* **1974**, *51*, 107–119. [CrossRef]
12. Chartier, D.; Muzeau, B.; Stefan, L.; Sanchez-Canet, J.; Monguillon, C. Magnesium alloys and graphite wastes encapsulated in cementitious materials: Reduction of galvanic corrosion using alkali hydroxide activated blast furnace slag. *MRS Adv.* **2016**, *1*, 4095–4101. [CrossRef]
13. El-Taib Heakal, F.; Tantawy, N.S.; Shehata, O.S. Impact of chloride and fluoride additions on surface reactivity and passivity of AM60 magnesium alloy in buffer solution. *Corros. Sci.* **2012**, *64*, 153–163. [CrossRef]
14. El-Taib Heakal, F.; Fekry, A.M.; Fatayerji, M.Z. Influence of halides on the dissolution and passivation behavior of AZ91D magnesium alloy in aqueous solutions. *Electrochim. Acta* **2009**, *54*, 1545–1557. [CrossRef]
15. Bradford, P.M.; Case, B.; Dearnaley, G.; Turner, J.F.; Woolsey, I.S. Ion beam analysis of corrosion films on a high magnesium alloy (Magnox Al 80). *Corros. Sci.* **1976**, *16*, 747–766. [CrossRef]
16. Gulbrandsen, E.; Taftø, J.; Olsen, A. The passive behaviour of Mg in alkaline fluoride solutions. Electrochemical and electron microscopical investigations. *Corros. Sci.* **1993**, *34*, 1423–1440. [CrossRef]
17. Boubon, R.; Deschanels, X.; Cabié, M.; Rébiscoul, D. Evolution of Corrosion Products Formed during the Corrosion of MgZr Alloy in Poral Solutions Extracted from Na-Geopolymers Used as Conditioning Matrix for Nuclear Waste. *Materials* **2020**, *13*, 4958. [CrossRef]
18. Lambertin, D.; Frizon, F.; Bart, F. Mg-Zr alloy behavior in basic solutions and immobilization in Portland cement and Na-geopolymer with sodium fluoride inhibitor. *Surf. Coat. Technol.* **2012**, *206*, 4567–4573. [CrossRef]
19. Rooses, A.; Steins, P.; Dannoux-Papin, A.; Lambertin, D.; Poulesquen, A.; Frizon, F. Encapsulation of Mg-Zr alloy in metakaolin-based geopolymer. *Appl. Clay Sci.* **2013**, *73*, 86–92. [CrossRef]
20. Rooses, A.; Lambertin, D.; Chartier, D.; Frizon, F. Galvanic corrosion of Mg-Zr fuel cladding and steel immobilized in Portland cement and geopolymer at early ages. *J. Nucl. Mater.* **2013**, *435*, 137–140. [CrossRef]
21. Barros, C.F.; Muzeau, B.; L'Hostis, V.; François, R. Impact of fluoride concentration on general corrosion of Mg-Zr alloy in a Na-geopolymer and alkaline solutions. *Corros. Sci.* **2020**, *176*, 109009. [CrossRef]
22. Steins, P.; Poulesquen, A.; Frizon, F.; Diat, O.; Jestin, J.; Causse, J.; Lambertin, D.; Rossignol, S. Effect of aging and alkali activator on the porous structure of a geopolymer. *J. Appl. Cryst.* **2014**, *47*, 316–324. [CrossRef]
23. Cyr, M.; Pouhet, R. Carbonation in the pore solution of metakaolin-based geopolymer. *Cem. Concr. Res.* **2016**, *88*, 227–235. [CrossRef]
24. Thomas, S.; Thomas, R.; Zachariah, A. *Microscopy Methods in Nanomaterials Characterization*; Elsevier: Amsterdam, Netherlands, 2017; ISBN 9780323461474.
25. Ricolleau, C.; Nelayah, J.; Oikawa, T.; Kohno, Y.; Braidy, N.; Wang, G.; Hue, F.; Florea, L.; Pierron Bohnes, V.; Alloyeau, D. Performances of an 80–200 kV microscope employing a cold-FEG and an aberration-corrected objective lens. *J. Electron. Microsc.* **2013**, *62*, 283–293. [CrossRef] [PubMed]
26. Dahmen, U.; Kim, M.G.; Searcy, A.W. Microstructural evolution during the decomposition of Mg(OH)2. *Ultramicroscopy* **1987**, *23*, 365–370. [CrossRef]
27. Song, G.L.; Unocic, K.A. The anodic surface film and hydrogen evolution on Mg. *Corros. Sci.* **2015**, *98*, 758–765. [CrossRef]
28. Qian, M.; Das, A. Grain refinement of magnesium alloys by zirconium: Formation of equiaxed grains. *Scr. Mater.* **2006**, *54*, 881–886. [CrossRef]
29. Bernard, J.; Caillat, R.; Darras, R. *Magnesium and Related Low Alloys*; CEA Report: Gif sur Yvette, France, 1959.
30. Reschka, S.; Gerstein, G.; Dalinger, A.; Herbst, S.; Nürnberger, F.; Zaefferer, S. Visualization and Observation of Morphological Peculiarities of Twin Formation in Mg-Based Samples After Electrically Assisted Forming. *Metallogr. Microstruct. Anal.* **2019**, *8*, 806–814. [CrossRef]
31. Maltseva, A.; Shkirskiy, V.; Lefèvre, G.; Volovitch, P. Effect of pH on Mg(OH) 2 film evolution on corroding Mg by in situ kinetic Raman mapping (KRM). *Corros. Sci.* **2019**, *153*, 272–282. [CrossRef]
32. Taheri, M.; Kish, J.R. Nature of surface film formed on mg exposed to 1 M NaOH. *J. Electrochem. Soc.* **2013**, *160*, 36–41. [CrossRef]
33. Ghali, E.; Dietzel, W.; Kainer, K.-U. General and Localized Corrosion of Magnesium Alloys: A Critical Review. *J. Mater. Eng. Perform.* **2004**, *13*, 7–23. [CrossRef]
34. Brady, M.P.; Rother, G.; Anovitz, L.M.; Littrell, K.C.; Unocic, K.A.; Elsentriecy, H.H.; Song, G.-L.L.; Thomson, J.K.; Gallego, N.C.; Davis, B. Film Breakdown and Nano-Porous Mg(OH) 2 Formation from Corrosion of Magnesium Alloys in Salt Solutions. *J. Electrochem. Soc.* **2015**, *162*, C140–C149. [CrossRef]
35. Steins, P.; Poulesquen, A.; Diat, O.; Frizon, F. Structural Evolution during Geopolymerization from an Early Age to Consolidated Material. *Langmuir* **2012**, *28*, 8502–8510. [CrossRef]
36. Dauphin-Ducharme, P.; Kuss, C.; Rossouw, D.; Payne, N.A.; Danis, L.; Botton, G.A.; Mauzeroll, J. Corrosion Product Formation Monitored Using the Feedback Mode of Scanning Electrochemical Microscopy with Carbon Microelectrodes. *J. Electrochem. Soc.* **2015**, *162*, C677–C683. [CrossRef]
37. Ribbe, P.H. Titanium, fluorine, and hydroxyl in the humite minerals. *Am. Mineral.* **1979**, *64*, 1027.
38. Vermilyea, D.A.; Kirk, C.F. Studies of Inhibition of Magnesium Corrosion. *J. Electrochem. Soc.* **1969**, *116*, 1487. [CrossRef]

39. Sevonkaev, I.; Goia, D.V.; Matijević, E. Formation and structure of cubic particles of sodium magnesium fluoride (neighborite). *J. Colloid Interface Sci.* **2008**, *317*, 130–136. [CrossRef] [PubMed]
40. Baum, M. The Role of Water Properties and Specific Ion Effects on the Evolution of Silica Nanoconfinement. 2018. Available online: http://www.theses.fr (accessed on 11 December 2020).
41. Aréna, H.; Rébiscoul, D.; Garcès, E.; Godon, N. Comparative effect of alkaline elements and calcium on alteration of International Simple Glass. *NPJ Mater. Degrad.* **2019**, *3*, 1–11. [CrossRef]
42. Gin, S.; Guittonneau, C.; Godon, N.; Neff, D.; Rebiscoul, D.; Cabí, M.; Mostefaoui, S. Nuclear glass durability: New insight into alteration layer properties. *J. Phys. Chem. C* **2011**, *115*, 18696–18706. [CrossRef]
43. Michelin, A.; Burger, E.; Rebiscoul, D.; Neff, D.; Bruguier, F.; Drouet, E.; Dillmann, P.; Gin, S. Silicate glass alteration enhanced by iron: Origin and long-term implications. *Environ. Sci. Technol.* **2013**, *47*, 750–756. [CrossRef]
44. Burger, E.; Rebiscoul, D.; Bruguier, F.; Jublot, M.; Lartigue, J.E.; Gin, S. Impact of iron on nuclear glass alteration in geological repository conditions: A multiscale approach. *Appl. Geochem.* **2013**, *31*, 159–170. [CrossRef]
45. Pokrovsky, O.S.; Schott, J.; Castillo, A. Kinetics of brucite dissolution at 25 °C in the presence of organic and inorganic ligands and divalent metals. *Geochim. Cosmochim. Acta* **2005**, *69*, 905–918. [CrossRef]
46. Taheri, M.; Phillips, R.C.; Kish, J.R.; Botton, G.A. Analysis of the surface film formed on Mg by exposure to water using a FIB cross-section and STEM-EDS. *Corros. Sci.* **2012**, *59*, 222–228. [CrossRef]